Integrated Wireless RFID Temperature Sensor for Biological Aortic Valve Prostheses

Federica Naccarata, *Graduate Student Member, IEEE,* Gaetano Marrocco, *Senior Member, IEEE*

***Abstract*—Body core temperature is one of the most reliable biometric indicators for monitoring the health status of a person. The gold standard in clinical settings is a highly invasive procedure involving the insertion of a catheter into the pulmonary artery, which receives blood directly from the core of the body. However, if a patient needs to host an Implanted Medical Device (IMD), a precise body core temperature measurement can be obtained without causing them additional discomfort, by adding communication and sensing capability to the IMD itself. This paper proposes a possible augmentation of a passive metal-free aortic valve prosthesis with a wrapped C-dipole provided by an RFID-based temperature sensor for batteryless and wireless temperature monitoring from the inside. A robust transcardiac link can be achieved with at least 24 dBm interrogation power by using a small on-skin reader antenna, which is also robust against moderate mutual misalignment among the two devices. The temperature sensing capability of a true sensorized valve, evaluated by means of a heated liquid phantom, demonstrated the possibility of sensing typical physiological temperature gradients with an average accuracy of less than 0.25 °C w.r.t. a reference thermocouple.**

***Index Terms*—Implantable Antennas, Radio Frequency Identification (RFID), Wireless Monitoring, Cyber-Prosthesis, Battery-Less.**

I. Introduction

The temperature of the body core is one of the most effective biometric indicators to track the health status of a person. The healthy human body temperature at rest is maintained at 37 ± 0.5 °C and, in the case of physical activity or disease, it spans within a small range of variation ($5-10$ °C), therefore, a precision of at least ±0.25 °C is required [1]. Collecting the temperature of the skin is not indicative of an accurate description of the thermal state of the human body [2], as it is highly influenced by environmental conditions that produce thermoregulating vasoconstriction. Instead, a reliable evaluation of core temperature involves invasive thermal probes, usually inserted into anatomical cavities (i.e., oral cavity, tympanic membrane, rectum, urinary bladder, nasopharynx, esophagus, and pulmonary artery) or even into surgical cavities of the body [3]. In clinical settings, the golden standard is an invasive and painful catheter inserted into the pulmonary artery [2] as it carries blood directly from the core of the body.

However, an accurate and reliable temperature measure could be achieved without additional discomfort for the patient if he needs to host an implanted medical device (IMD), which could therefore be provided with a *in-situ* temperature sensor and wireless communication capabilities [4]. In particular, an aortic valve prosthesis, which is mainly required to restore transvalvular pressure gradients and the ideal hemodynamic condition of blood flow [5], is naturally in contact with blood close to the heart and, therefore could collect the temperature at the right place without artifacts. In addition to providing information on monitoring the temperature of the "core", this capability could also give a valid indication of the viscosity of the blood and, therefore, of the tendency to develop stenosis [6], [7], which is a very common disease at the heart valve level. Furthermore, in critically ill patients, the core temperature is correlated with the heart rate [8].

The addition of thermometer functionality is straightforward when active IMDs are involved, such as implantable loop recorders, leadless pacemakers, and subcutaneous cardioverter defibrillators [9]. Instead, in the case of simpler passive IMDs, such as cardiac valves, stents, and implantable blood flow sensor attached to the ascending aorta [5], the added sensor capability must not hinder main mechanical operations or alter the dynamics of blood fluid [10]. Accordingly, only minimal changes to the IMD structure are tolerated, thus excluding the possibility of complex electronics and batteries.

Very recently, several options were explored to augment a passive IMD with sensors by resorting to Radio Frequency IDentification (RFID) technology in the UHF band ($860-960$ MHz) as a batteryless communication platform. For example, an application to a bone plate fixture, which was converted into an antenna "of opportunity" capable of measuring the local temperature to detect the early sign of infections, was given in [11]. An integrated RFID circuit (IC) was also integrated into an orthopedic prosthesis to detect cracks [12] and monitor temperature [13] and in a dental implant [14] for future applications to monitor tooth grinding. Pioneering applications in vascular IMDs refer to a stent [15] to identify the onset of resthenosis and in [16] for non-invasive resthenosis treatments using a radiofrequency (RF) electro-thermo-mechanical technique for wireless revascularization.

More specifically, the first attempt to augment a tricuspid valve with an RFID IC, using the embedded metal stent as a *structural* loop antenna, was very recently presented by the authors in [17]. Preliminary simulations and measurements on a liquid body phantom allowed the transcardiac communication link to be evaluated with an epidermal interrogating antenna placed on the thorax. More recently, we generalized the idea to a metal-free valve in the conference paper in [18]. A curvilinear dipole (C-dipole) was wrapped around the semi-rigid stent of the valve, whereas the IC for communication and sensing is housed on one of the cuspids, with minimal change to the IMD.

The authors are with the Pervasive Electromagnetics Lab, University of Rome Tor Vergata, Via del Politecnico 1, Rome 00133, Italy (e-mail: naccarata@ing.uniroma2.it, gaetano.marrocco@uniroma2.it)

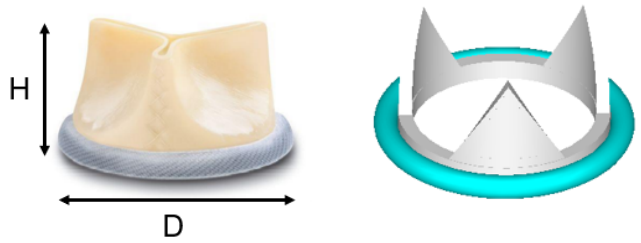

(a) (b)

Fig. 1. (a) LivaNova metal-free biological aortic valve prosthesis (model: Crown PRT [19] D=21 mm, H=11 mm) and (b) simplified electromagnetic model of the valve.

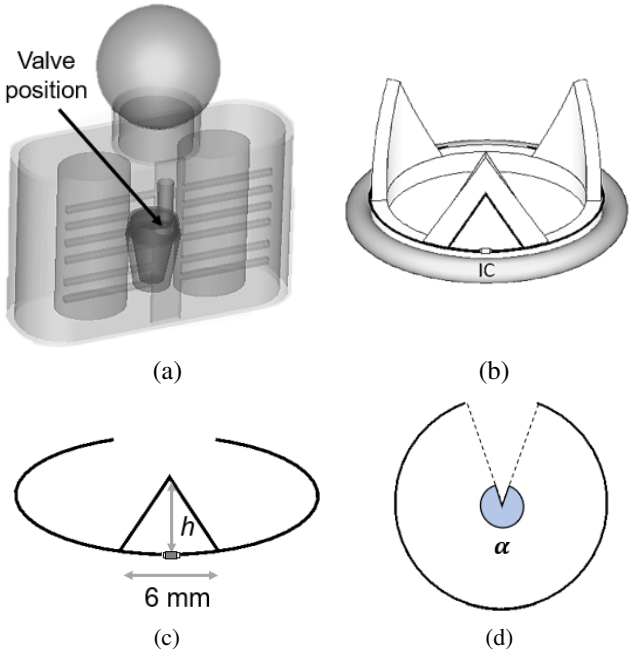

(a) (b) (c) (d)

Fig. 2. (a) Model of the thorax for electromagnetic simulations. (b) Antenna mounted on the valve. Antenna layout: (c) C-dipole with triangular T-match, (d) aperture angle of the C-dipole.

This paper is an extension of the above contribution to demonstrate for the first time the possibility of using the antennified tricuspid valve to collect reliable temperature data from the inside of the body, without any battery onboard. In particular, we will show how to calibrate the embedded sensor by means of a reference probe and a Bland-Altman analysis. The system will therefore be tested to measure two typical metabolic thermal transients.

The paper is organized as follows. Section II introduces the cardiac valve model and the antenna layout for integration into the IMD. The transcardiac link is then evaluated in Section III, while the electromagnetic performance of a manufactured prototype on a real valve is resumed in Section IV. Finally, Section V reports the experimental results from temperature measurements during some fever-like thermal gradients compared to those from a reference probe.

II. Valve-Integrated Antenna Harvester

A. Valve model

Biological valve prostheses are made up of animal-derived leaflets (human, porcine, or bovine tissues) with a semi-lunar shape, securely attached to a supporting structure, namely the stent, provided with cusps [20]. In the case of a metal-free valve, the stent is made of polymeric materials and coated with a dielectric fabric, generally polyester (an example in Fig. 1 (a)). The stent is then attached to a circular base ring, typically made of silicone rubber, to easily sew the device to the native aortic annulus. For simplicity of simulation, the prosthetic device is hereafter emulated by a polymeric framework ($\varepsilon = 3.7$, $tan\delta = 0.005$ [21]) with three cusps, enveloped by a dielectric layer ($\varepsilon = 2.1$, $tan\delta = 0.0035$ [22]) and a basal circular silicone suture ring ($\varepsilon = 2.2$, $\sigma = 0.005$ S/m), as shown in Fig. 1 (b).

Numerical simulations are performed by using the Finite Element Method (FEM) in CST Microwave Studio, resorting to a simplified but heterogeneous anthropomorphic human thorax model (skin, fat, muscle) that comprises elliptical cylinders with internal structure such as the ribs, sternum, and lung, from [23] (Fig. 2 (a)). The electrical properties of human tissues at 900 MHz are listed in Tab. I [24]. The device is assumed to be placed in the aorta, at 7 cm depth. The heart and aortic vessel are always considered to be filled with blood, as a conservative electromagnetic scenario.

B. Sensing-oriented RFID IC

The sensor-oriented IC selected for this application is the Axzon Magnus-S3 [25]. It is equipped with an integrated solid-state temperature sensor, allowing minimization of the required electronic components and costs. It provides an operating range -40 °C $\leq T \leq 85$ °C with a resolution 0.13 °C. According to the data sheet [25], the temperature measurement is reliable when the value of the Power-on-Chip (PoC) code [1] falls within the $13 \leq PoC \leq 18$ range. However, the application of a correction method [1] allows us to take advantage of a larger interval of $13 \leq PoC \leq 30$. The IC has a power sensitivity $P_{IC} = -13.6$ dBm. The RF admittance has a fixed real part $G_{IC} = 0.5$ mS at 900 MHz [25], while the susceptance B_{IC} is automatically adjusted (auto-tuning capability) to account for any potential mismatch with the antenna caused by variable

[1]The PoC code is a 5-bit value returned by the IC during the RFID interrogation, indicating the amount of power collected by the IC.

TABLE I
Electrical properties of tissues at 900 MHz.

	$\sigma[\frac{S}{m}]$	ε_r
Aorta	0.70	44.78
Blood	1.54	61.36
Bone	0.14	12.90
Cardiac Muscle	1.23	59.89
Fat	0.05	05.46
Lung	0.46	22.00
Muscle	0.94	55.00
Skin	0.86	41.40

boundary conditions, maximizing the harvested power. The equivalent circuit of the IC can be modeled as a resistor in parallel with a capacitor ladder with a total capacitance $C_{IC} = C_{IC_0} + sC_{IC_{step}}$ ranging from a minimum value C_{IC_0} to a maximum value [26]. The variable susceptance of the IC is derived from the auto-tuning condition $|B_A + \omega C_{IC}| = 0$, being B_A the input susceptance of the antenna. In this way, the power transfer coefficient τ, that is the fraction of RF power harvested by the antenna and then transferred to the IC, is expressed by accounting for the auto-tuning condition in the linear and saturation ranges of the IC [26]:

$$\tau(f) = \begin{cases} \frac{4G_{IC}G_A}{\left|G_{IC}+G_A+j\left(B_A+\omega C_{IC_0}\right)\right|^2} \\ \text{if } B_A > -\omega C_{IC_0} \\ \frac{4G_{IC}G_A}{(G_{IC}+G_A)^2} \\ \text{elsewhere} \\ \frac{4G_{IC}G_A}{|G_{IC}+G_A+j[B_A+\omega(C_{IC-0}+sC_{IC_s tep})]|^2} \\ \text{if } B_A < -\omega(C_{IC_0} + s_{max}C_{IC_{step}}) \end{cases} \quad (1)$$

where G_{IC} and G_A are the conductance of the IC and antenna.

C. Antenna Layout

The antenna that works as an energy harvester for the integrated temperature sensor, which will be embedded in the dielectric coating, is a thin C-dipole, made of a copper wire of 0.2 mm diameter, wrapped around the outer perimeter of the valve. Therefore, the conducting element is isolated from its surrounding tissues through the dielectric coating. The dipole is connected to the RFID IC by a triangular T-match transformer, housed in one of the cuspids, which adds some degree of freedom for the impedance matching of the antenna with the IC (Fig. 2 (b)). The free parameters to be optimized to maximize communication performance are the angular aperture α of the C-dipole and the height *h* of the triangular T-match (Fig. 2 (c), (d)).

D. Parametric Analysis

The antenna design is organized into two steps. First, assuming the C-dipole in the transmitting mode, the angular size α is optimized to maximize the active power (the real part of the Poynting vector flux) flowing through an area of 4 cm x 4 cm on the thorax where the interrogating antenna will be placed. Then, by fixing α, impedance matching is achieved by varying the height *h* of the triangular T-match transformer. In this second step, the parameter to be optimized is the power transfer coefficient $\tau(f)$.

The resulting peak of normalized power (-34.8 dB, Fig. 3 (a)) occurs for $\alpha = 320°$. Then, Fig. 3 (b) shows the power transfer coefficient, accounting for the IC auto-tuning as in Eq. 1, which exhibits a typical flat broadband behavior with τ (900 MHz) > 0.8 for any considered h. However, the best centered profile in the RFID-UHF band corresponds to $h = 4.5$ mm.

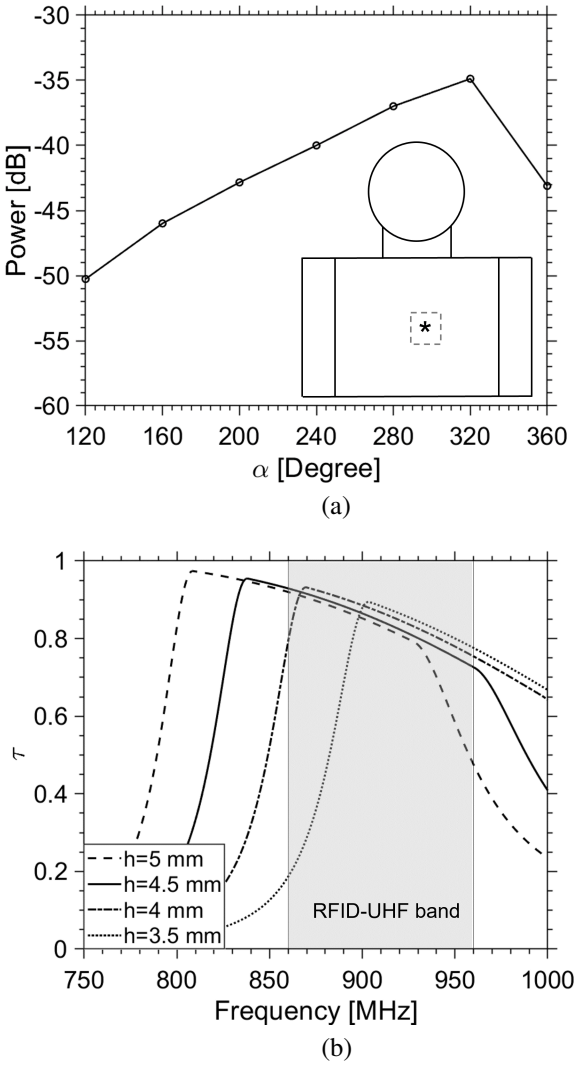

Fig. 3. (a) Real part of the power at 900 MHz vs. the aperture angle of the C-dipole. Inset of the reference model of the thorax with the asterisk corresponding to the position of the valve and area of 4 cm x 4 cm where the interrogating antenna will be placed. (b) Simulated frequency profiles of the power transfer coefficient for different values of the height of the triangular T-match.

The antennified valve generates an electric field outside the thorax with a predominant horizontal orientation (Fig. 4). In the far-field it would produce a linear polarization (LP) with a 40 dB axial ratio.

III. Evaluation of the Transcardiac Link

The complete link between the valve-integrated antenna and the external interrogator is modeled here as a lossy two-port network [27], described by the Admittance Matrix $[Y_{i,j}]$ where port 1 (input) and port 2 (output) correspond to the reader antenna and the terminals of the implanted device, respectively. The performance parameter of the communication link is the Transducer Power Gain G_T, which is the ratio between the

power provided by the reader to the IC ($P_{R\to T}$) and the power available from the generator ($P_{av,R}$) [28]. It can be defined in terms of admittance [29] as

$$G_T = \frac{P_{R\to T}}{P_{av,R}} = \frac{4G_g G_{IC}|Y_{12}|^2}{|(Y_{11}+Y_g)(Y_{22}+Y_{IC})-Y_{12}^2|^2} \quad (2)$$

where $Y_g = G_g + jB_g$ is the internal admittance of the reader.

Considering the maximum output power that the reader can provide, namely $P_{av,R} = 1$ W, the power margin M of the transcardiac link (in dB) is defined as

$$M = G_T + P_{av,R} - P_{IC} - M_0 \geq 0 \quad (3)$$

where M_0 is an additional safety margin of 3 dB to take into account the unpredictable factors of the real arrangement. The transcardiac link is guaranteed when $M \geq 0$ dB. From Eq. (3), the minimum useful value of the Transducer Power Gain to establish communication is therefore $G_T \geq -40.6$ dB.

A. Numerical Evaluation of the Transcardiac Link

To estimate the realistic communication performance of the valve-integrated antenna designed through the above two-port model, we will refer to a reader's antenna placed on the thorax that is a linearly polarized microstrip slot (inset Fig. 5), with layout and dimensions from [17]. Even though the use of a Circular Polarized (CP) reader antenna would have provided a more robust link versus imperfect orientation among antennas, the combination of CP (reader) and LP (implant) is expected to produce 3 dB polarization loss in the transcutaneous link with respect to an optimal LP-LP link having perfect orientation between antennas. This means that a higher power would be required to establish a LP-CP link with a relevant impact on the power source and, above all, the compliance with the Specific Absorption Rate (SAR) since a larger amount of power will be overall delivered in the body. We therefore assume that the orientation of the reader antenna could be adjusted, in the real life, by hand according to a trial&error procedure to match the optimal orientation among antennas, thus minimizing the transmitted power and, accordingly, the SAR.

The reader antenna is partially insulated from the thorax by a silicone layer (thickness 2 mm). The patch is well matched to 50 Ω when applied onto the thorax with a reflection coefficient less than -15 dB in the $867-868$ MHz EU RFID band (see [17]).

Fig. 5 shows the calculated G_T over frequency. The flat profile in a wide frequency band is due to the auto-tuning behavior of the IC. In particular, the power margin $M \geq 0$ dB fully comprises the worldwide RFID-UHF band. At 900 MHz, a notable value of $M = 6$ dB indicates the possibility of implementing a reliable communication link via backscattering, with a high power margin.

B. Electromagnetic Exposure Considerations

The compliance of the above link with constraints of electromagnetic exposure for the human body during the interrogation of the valve by the external antenna, can be borrowed from the detailed analysis in [17]. By considering the safety regulations, the SAR averaged onto 10 g must be less than 2 W/kg. The SAR delivered by the reader antenna inside the thorax respects this restriction when $P_{av,R} = 1$ W for a duty cycle (D), i.e. the interrogation rate, of $D = 0.11$.

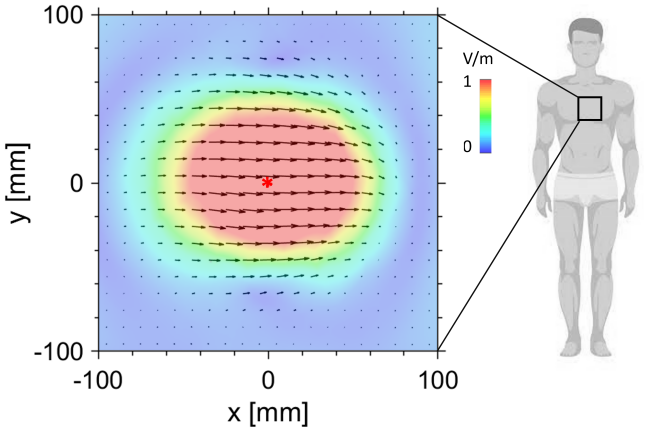

Fig. 4. Simulated normalized E-field over a surface parallel to the thorax, at 2 cm from it. The red asterisk identifies the position of the valve.

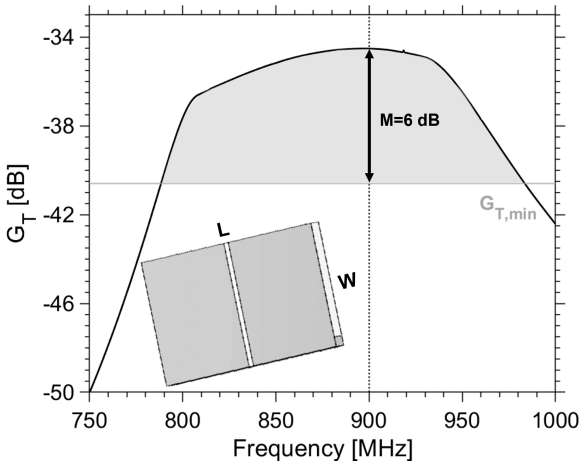

Fig. 5. Simulated Transducer Power Gain of the two-port network that identifies the near-field reader-valve interaction. The power margin is evaluated for $P_{av,R}$=1 W. Inset: layout of the reader antenna ($L = 40$ mm, $W = 25$ mm, other sizes reported in [17]).

IV. Prototype and Electromagnetic Characterization

We had the opportunity to integrate a prototype of the C-dipole into a real tricuspid valve to validate the aforementioned numerical analysis by means of electromagnetic characterization and then to perform temperature measurements.

A. Fabrication

For the sake of simplicity, the triangular T-match was manufactured on a 0.8 mm thick FR4 PCB (trace width 0.4 mm) by means of a milling machine. The C-dipole was made of copper wires and their terminals were soldered to the PCB.

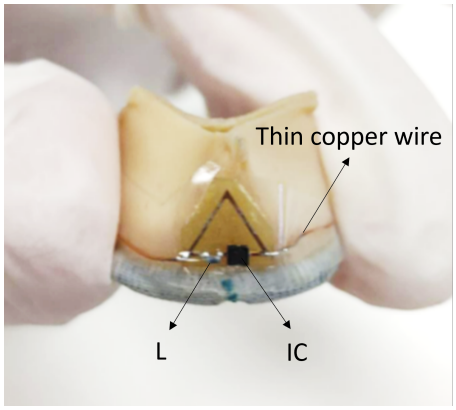

(a)

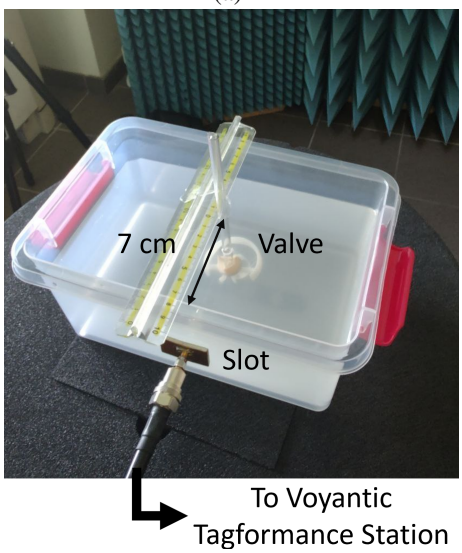

(b)

Fig. 6. Experimental setup involving: (a) assembled prototype placed on the real valve and (b) liquid phantom mimicking the thorax.

To have some additional degree of freedom in impedance tuning, a series inductor ($L = 2.8$ nH) was added. The IC and inductor were mounted on the traces by a pick&place machine using a solder paste (conductive epoxy CW2400 by Chemtronics). Electromagnetic insulation is achieved by sandwiching encapsulation with a PET film (thickness 0.1 mm, $\varepsilon = 2.1$, $\sigma = 0.0002$ S/m) [12]). Finally, the assembled prototype was placed on the valve, as shown in Fig. 6 (a). For a more realistic application, the copper trace could be directly transferred by laser cutting or inkjet printing on the polymeric stent of the valve.

B. Link measurement

The human thorax was emulated by a PET box (thickness 2 mm) filled with a homogeneous liquid mixture ($\varepsilon = 54$, $\sigma = 1.05$ S/m [30]) of overall equivalent dielectric properties similar to muscle. To emulate real implantation, the sensorized valve was drowned in the phantom at a depth of 7 cm. The external reader antenna was then applied to the exterior surface of the container, without the silicone layer due to the presence of the PET box (Fig. 6 (b)). The interrogating antenna and the valve are perfectly aligned as in Fig. 6 (b) so that the T-match IC is in front of the slot.

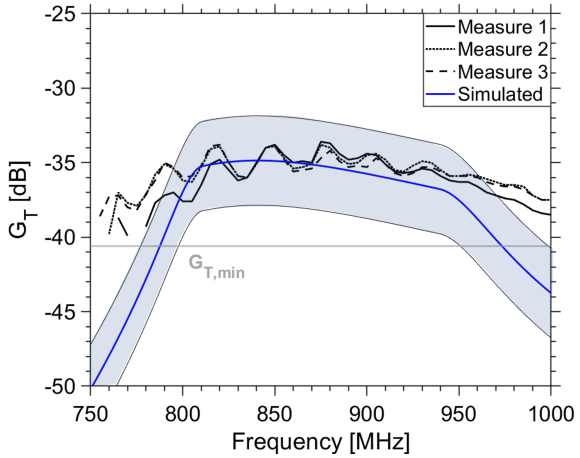

Fig. 7. Frequency profile of the measured and simulated G_T when the antennified-valve is immersed at 7 cm depth in the liquid phantom. The ± 3 dB shadow region accounts for manufacturing imperfections.

The reader antenna was connected to the Voyantic Tagformance station to perform a wideband electromagnetic characterization in the $750 - 1000$ MHz frequency range. Measurements of the Transducer Power Gain were repeated three times and compared with the results of the corresponding simulated setup. Fig. 7 shows the frequency profiles of the measured G_T that compare well with the simulated outcome, with a difference of less than 3 dB in a wide frequency band. The measured data are higher than the minimum threshold value of G_T, which is useful for establishing the through-the-body communication link throughout the UHF-RFID band. Visible oscillations are caused by the IC auto-tuning feature, which automatically modifies its internal susceptance, frequency by frequency, to keep the antenna-IC impedance matching stable [29].

C. Tolerance to Misalignment

During the surgical intervention, the valve could not have been properly oriented so that the sensorized cuspid looks toward the thorax, and then, after implantation, the interrogating antenna could not be placed properly in the best place of the thorax. The following experiments quantify the robustness of the link to possible valve-interrogator misalignment. We considered four possible arrangements with respect to the perfect alignment (as in Fig. 6 (b)), namely *i*) horizontal shift; *ii*) vertical shift, *iii*) rotation of the reader antenna, and *iv*) rotation of the valve around the virtual aorta when the external antenna is fixed in the optimal position. The results of the measurements are reported in Fig. 8 and in Fig. 9. The telemetry system appears to be resilient and maintains a good power margin over a broad band in the case of $\pm$ 2 cm of displacement. However, in the case of angular displacements of the reader antenna and the sensorized valve, the link is less robust. To at least guarantee a $M = 1$ dB margin, only

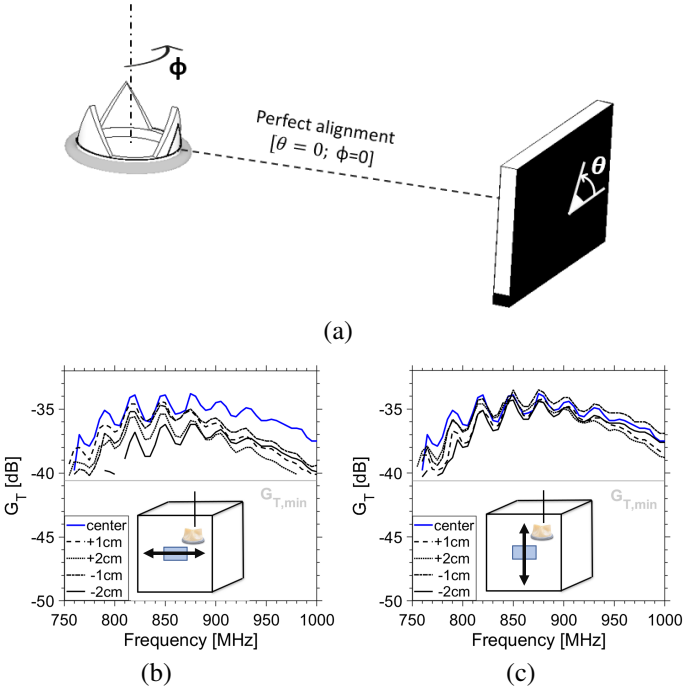

Fig. 8. (a) Mutual position of antennas in case of perfect alignment and indication of reference angles. Measured Transducer Power Gain G_T in case of: (a) horizontal and (b) vertical misalignment.

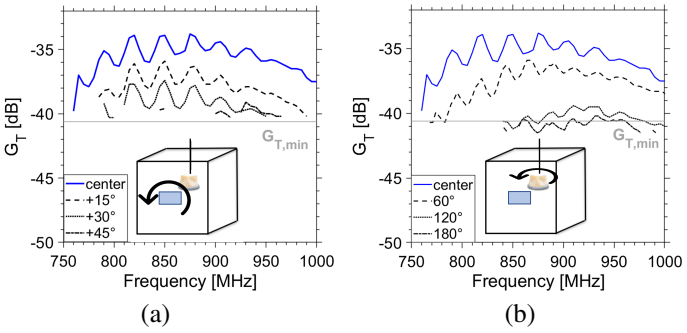

Fig. 9. Measured Transducer Power Gain G_T in case of: (a) θ (reader rotation) and (b) Φ (valve rotation) angular displacements.

rotations up to 30° are allowed for the reader antenna and 60° for the valve.

V. Application To Temperature Measurement

The last experimental campaign aims to quantify the capability of the sensor-oriented IC to detect the local temperature. First of all, since the temperature sensor is embedded inside the IC and insulated by the PET film, its temperature conductivity is lower and thus requires calibration as in [31].

A. Calibration

The sensorized valve was drowned in liquid and a calibrated k-type thermocouple probe was also placed close to the IC to capture the *reference* temperature. The probe was sampled using a 16 bit acquisition device (MONODAQ-U-X, by Devesoft, [32]). The interrogator was the ThingMagic M6E reader

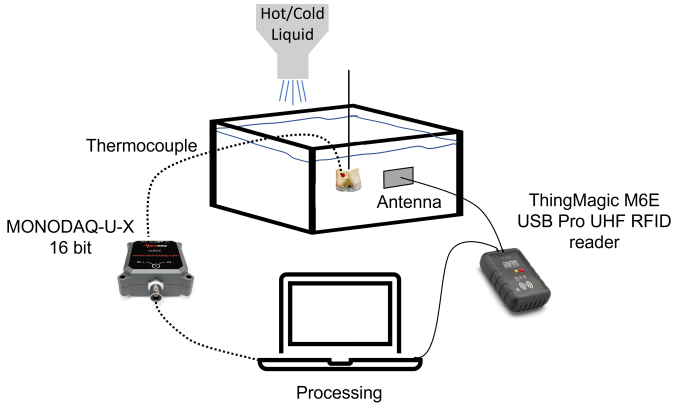

Fig. 10. Scheme of the experimental temperature measurement setup.

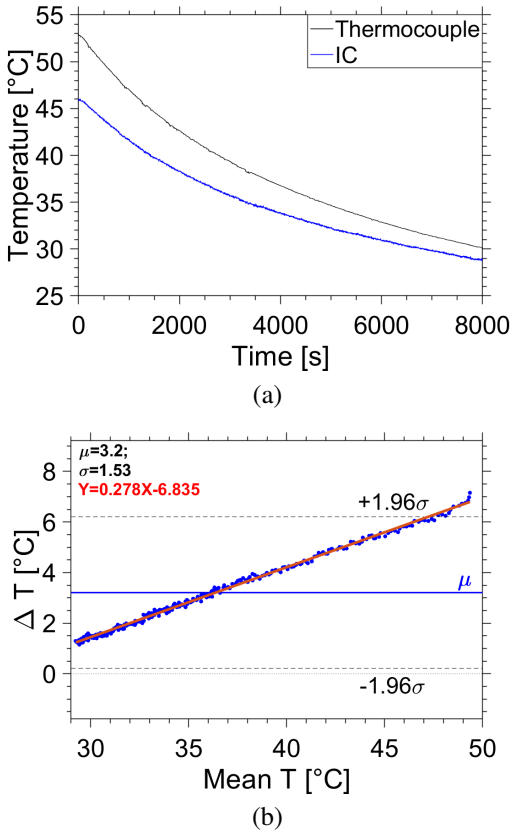

Fig. 11. (a) Measurements by a polymeric valve equipped with a sensor-oriented RFID IC temperature sensor. Raw temperatures are displayed in comparison with a reference thermocouple. (b) Bland-Altman diagrams with indication of 95% limit of agreement, bias, and linear regression of the dataset in case of no calibration.

connected to the microstrip-slot antennas as before (setup in Fig. 10). For calibration purposes, the PET box was filled with 3 L of physiological solution (0.9% NaCl) at 55 °C. Data were recorded every second during cooling to 30 °C, as in [31]. The temperature profiles collected by the two thermometers are shown in Fig. 11 (a). The two-hour test revealed, as expected, that the RFID sensor follows the thermocouple but with variable offset. More in detail, the Bland-Altman diagram in Fig. 11 (b) shows that there is a linear offset among the two

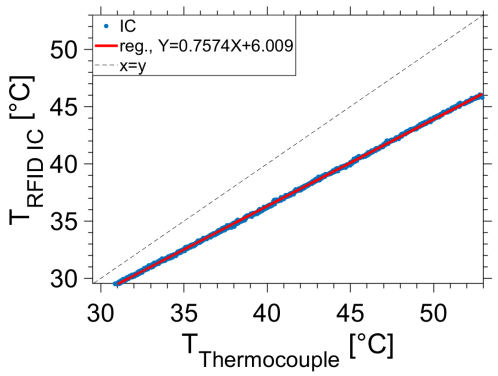

(a)

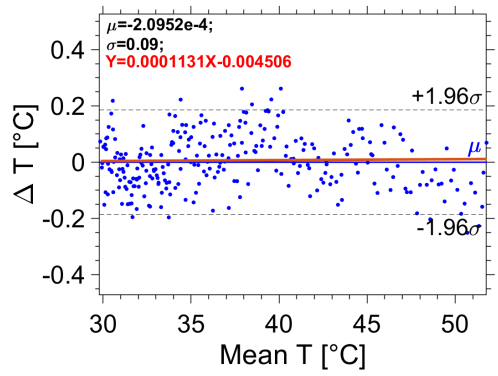

(b)

Fig. 12. (a) RFID data vs. reference thermocouple with indication of linear regression. (b) Bland-Altman diagrams with indication of 95% limit of agreement, bias, and linear regression of the dataset in case of calibration.

sets of data that can therefore be corrected by means of linear regression (parameters $a = 0.7574$; $b = 6.009$) (Fig. 12 (a)). RFID IC sensor readings are linearly correlated with probe reference temperature, with a determination coefficient equal to $R^2 = 0.9998$. The calibrated RFID temperature ($\widetilde{T}_{RFID\ IC}$) can therefore be evaluated as

$$\widetilde{T}_{RFID\ IC} = 1.32\ x\ T_{RFID\ IC} - 7.934. \quad (4)$$

The corrected data in Fig. 12 (b) now exhibit a negligible bias ($\mu \approx 0$ °C) and standard deviation $\sigma = 0.09$ °C, leading to an approximately ± 0.18 °C difference between the two thermometers (95% degree of agreement) in almost all measured range.

B. Measurement of febrile-like transients

Fig. 13 shows two temperature profiles, emulating febrile-like gradients in a liquid phantom. The temperature of the liquid is varied by adding hot/cold liquid in a controlled manner through a funnel. In the first, the temperature increased by 3 °C from a value corresponding to mild hypothermia (34.5 °C). The second temperature profile then reproduces an increase in temperature in case of fever, starting from a typical basal temperature of the body (36.6 °C) under

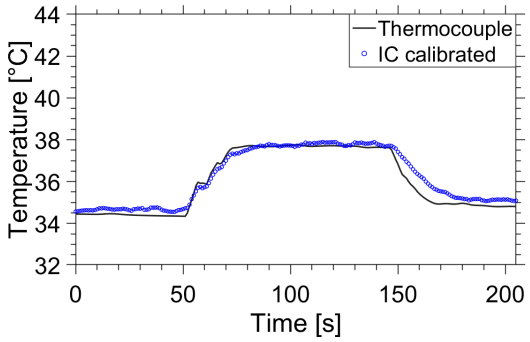

(a)

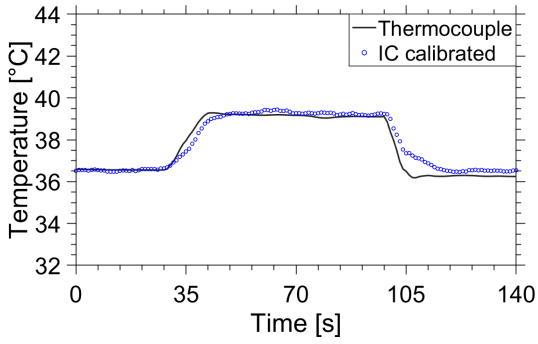

(b)

Fig. 13. Temperature measurements of febrile-like transients starting from: (a) mild hypothermia state; (b) healthy physiological state.

healthy conditions. By applying the calibration as above, the temperature returned from the valve prosthesis by wireless reading is in good agreement with the wired thermocouple probe, with an average difference of less than 0.25 °C.

VI. Conclusions

We have proposed a tightly integrated RFID sensor suitable for artificial metal-free tricuspid valves. Numerical simulations and experimental characterization of communication performance demonstrated that a stable transcardiac link can be established and that it is little sensitive to reader-sensor misalignment. Even though the antenna design has been referred to a specific valve model, nevertheless, the auto-tuning capability of the IC and the T-match can easily adjust the antenna impedance to valves of different sizes and shapes. Moreover, in a more realistic application, the copper trace could be directly transferred by laser cutting or inkjet printing on the polymeric stent of the valve. The results of preliminary experimental tests on the measurement of realistic temperature profiles are well in agreement with the reference probe with a difference of less than 0.25 °C, so that the sensorized device could be more than adequate to capture the physiological variation of the core temperature related to fever and other health abnormalities.

Acknowledgement

The work was partially supported by Rome Technopole in the framework of the National Recovery and Resilience Plan (NRRP), NextGenerationEU.

REFERENCES

[1] F. Camera and G. Marrocco, "Electromagnetic-based correction of bio-integrated RFID sensors for reliable skin temperature monitoring," *IEEE Sensors Journal*, vol. 21, no. 1, pp. 421–429, 2021.

[2] H. Hymczak *et al.*, "Core temperature measurement—principles of correct measurement, problems, and complications," *International Journal of Environmental Research and Public Health*, vol. 18, no. 20, p. 10606, 2021.

[3] D. S. Moran and L. Mendal, "Core temperature measurement: methods and current insights," *Sports Medicine*, vol. 32, pp. 879–885, 2002.

[4] A. Kiourti, "RFID antennas for body-area applications: from wearables to implants," *IEEE Antennas and Propagation Magazine*, vol. 60, no. 5, pp. 14–25, 2018.

[5] B. Vennemann, D. Obrist, and T. Rösgen, "A smartphone-enabled wireless and batteryless implantable blood flow sensor for remote monitoring of prosthetic heart valve function," *PLoS One*, vol. 15, no. 1, p. e0227372, 2020.

[6] C. Kumawat, B. Sharma, and K. Mekheimer, "Mathematical analysis of two-phase blood flow through a stenosed curved artery with hematocrit and temperature dependent viscosity," *Physica Scripta*, vol. 96, no. 12, p. 125277, 2021.

[7] S.-R. Yan *et al.*, "Numerical investigation of non-newtonian blood flow within an artery with cone shape of stenosis in various stenosis angles," *Computer methods and programs in biomedicine*, vol. 192, p. 105434, 2020.

[8] M. E. Broman *et al.*, "The relationship between heart rate and body temperature in critically ill patients," *Critical Care Medicine*, vol. 49, no. 3, pp. e327–e331, 2021.

[9] A. Joury *et al.*, "Leadless and wireless cardiac devices: the next frontier in remote patient monitoring," *Current Problems in Cardiology*, p. 100800, 2021.

[10] K. B. Chandran, S. E. Rittgers, and A. P. Yoganathan, *Biofluid mechanics: the human circulation*. CRC press, 2006.

[11] P. Avaltroni, S. Nappi, and G. Marrocco, "Antennifying orthopedic bone-plate fixtures for the wireless monitoring of local deep infections," *IEEE Sensors Journal*, vol. 21, no. 18, pp. 21 012–21 021, 2021.

[12] S. Nappi *et al.*, "A fractal-RFID based sensing tattoo for the early detection of cracks in implanted metal prostheses," *IEEE Journal of Electromagnetics, RF and Microwaves in Medicine and Biology*, 2021.

[13] A. Vena *et al.*, "RFID based implant for knee prosthesis 2.0," in *2022 IEEE 12th International Conference on RFID Technology and Applications (RFID-TA)*, 2022, pp. 105–108.

[14] N. Panunzio *et al.*, "Cyber-tooth: antennified dental implant for RFID wireless temperature monitoring," in *2021 IEEE International Conference on RFID Technology and Applications (RFID-TA)*. IEEE, 2021, pp. 211–214.

[15] C. Occhiuzzi, G. Contri, and G. Marrocco, "Design of implanted RFID tags for passive sensing of human body: the STENTag," *IEEE Transactions on Antennas and Propagation*, vol. 60, no. 7, pp. 3146–3154, 2012.

[16] Y. X. Ang, A. Z. M. Khudzari, and M. S. M. Ali, "Non-invasive treatment for coronary in-stent restenosis via wireless revascularization with nitinol active stent," *IEEE Transactions on Biomedical Engineering*, vol. 68, no. 12, pp. 3681–3689, 2021.

[17] F. Naccarata *et al.*, "Wireless and zero-power trans-cardiac link with antennified aortic valve bioprostheses," *IEEE Journal of Electromagnetics, RF and Microwaves in Medicine and Biology*, pp. 1–9, 2022.

[18] F. Naccarata, C. Occhiuzzi, R. Verzicco, and G. Marrocco, "Minimally invasive antennas into aortic valve prostheses for RFID-based trans-cardiac links," in *2022 IEEE 12th International Conference on RFID Technology and Applications (RFID-TA)*, 2022, pp. 176–179.

[19] LivaNova., "Crown PRT," available on line. Accessed: Oct. 01, 2022. [Online]. Available: https://livanovamediaprod.azureedge.net/livanova-media/livanova-public/media/resources01/ous_only_livanova_crown-prt_prod_broch_eu_re0210200-f.pdf?ext=.pdf

[20] P. Blanke *et al.*, "Computed tomography assessment for transcatheter aortic valve in valve implantation: the vancouver approach to predict anatomical risk for coronary obstruction and other considerations," *Journal of cardiovascular computed tomography*, vol. 10, no. 6, pp. 491–499, 2016.

[21] Technical Products, Inc., "Delrin® homopolymer material specifications," available on line. Accessed: Nov. 1, 2022. [Online]. Available: https://www.technicalproductsinc.com/pdf/Specs/Delrin%20Specs.pdf

[22] J. Lesnikowski, "Dielectric permittivity measurement methods of textile substrate of textile transmission lines," *Przeglad Elektrotechniczny*, vol. 88, no. 3A, pp. 148–151, 2012.

[23] M. Gagliardi *et al.*, "How to transform an aortic valve prostheses into an UHF antenna for the RFID-based wireless monitoring of the cardiac health," in *16th European Conference on Antennas and Propagation (EUCAP), Madrid, 2022.*

[24] IFAC-CNR., "Calculation of the dielectric properties of body tissues in the frequency range 10 Hz - 100 GHz," available on line.Accessed: Feb. 20, 2022. [Online]. Available: http://niremf.ifac.cnr.it/

[25] Magnus S3 Axzon, accessed: May. 2, 2022. [Online]. Available: https://axzon.com/rfm3300-d-magnus-s3-m3d-passive-sensor-ic/

[26] F. Naccarata, G. M. Bianco, and G. Marrocco, "Sensing performance of multi-channel RFID-based finger augmentation devices for Tactile Internet," *IEEE Journal of Radio Frequency Identification*, 2022.

[27] S. J. Orfanidis, *Electromagnetic Waves and Antennas*. [Online]. Available: http://eceweb1.rutgers.edu/ orfanidi/ewa/

[28] G. Monti *et al.*, "Wireless power transfer strategies for medical implants: Focus on robustness and em compatibility," *IEEE Microwave Magazine*, vol. 22, no. 9, pp. 28–41, 2021.

[29] G. M. Bianco, S. Amendola, and G. Marrocco, "Near-field constrained design for self-tuning UHF-RFID antennas," *IEEE Transactions on Antennas and Propagation*, vol. 68, no. 10, pp. 6906–6911, 2020.

[30] Speag Swiss, accessed: May. 5, 2022. [Online]. Available: https://speag.swiss/components/materials-liquids/msl/

[31] Q. Hua *et al.*, "Design and in-vivo test of battery-free implantable temperature sensor based on magnetic resonant wireless power transfer," in *2022 IEEE Nordic Circuits and Systems Conference (NorCAS)*, 2022, pp. 1–6.

[32] Monodaq, available on line. Accessed: Dec. 20, 2022. [Online]. Available: https://www.monodaq.com/shop/media/uploads//MonoDAQ-E-DO4Datasheetv1.0.pdf